

Research Article

Nonlinear Analysis for the Crack Control of SMA Smart Concrete Beam Based on a Bidirectional B-Spline QR Method

Yan Li,¹ Tian-jing Mo,¹ Shuang-bei Li ^{1,2} Qing-guo Liang,³ Jian-ping Li,⁴ and Rong Qin¹

¹College of Civil Engineering and Architecture, Guangxi University, Nanning 530004, China

²The Key Laboratory of Disaster Prevention and Structural Safety of the Education Ministry, Guangxi University, Nanning 530004, China

³Electric Power Research Institute of Guangxi Power Grid Co., Ltd., Nanning 530023, China

⁴Department of Geotechnical Engineering, Tongji University, Shanghai 200092, China

Correspondence should be addressed to Shuang-bei Li; lsbwh90@163.com

Received 1 August 2017; Revised 10 November 2017; Accepted 16 November 2017; Published 11 January 2018

Academic Editor: Fabrizio Greco

Copyright © 2018 Yan Li et al. This is an open access article distributed under the Creative Commons Attribution License, which permits unrestricted use, distribution, and reproduction in any medium, provided the original work is properly cited.

A bidirectional B-spline QR method (BB-sQRM) for the study on the crack control of the reinforced concrete (RC) beam embedded with shape memory alloy (SMA) wires is presented. In the proposed method, the discretization is performed with a set of spline nodes in two directions of the plane model, and structural displacement fields are constructed by the linear combination of the products of cubic B-spline interpolation functions. To derive the elastoplastic stiffness equation of the RC beam, an explicit form is utilized to express the elastoplastic constitutive law of concrete materials. The proposed model is compared with the ANSYS model in several numerical examples. The results not only show that the solutions given by the BB-sQRM are very close to those given by the finite element method (FEM) but also prove the high efficiency and low computational cost of the BB-sQRM. Meanwhile, the five parameters, such as depth-span ratio, thickness of concrete cover, reinforcement ratio, prestrain, and eccentricity of SMA wires, are investigated to learn their effects on the crack control. The results show that depth-span ratio of RC beams and prestrain and eccentricity of SMA wires have a significant influence on the control performance of beam cracks.

1. Introduction

Cracking is one of the main nonlinear characteristics of reinforced concrete (RC) structures. Once tiny cracks are created, they may expand and lead to accelerated corrosion of steel bars, which reduce structural reliability and durability. And the large cracks that exceed the limit may cause the structural failure [1]. Therefore, the durability and carrying capacity of structures can be effectively improved by controlling the development of cracks. With the continuous progress of material science, smart concrete provides a new and effective method to solve this problem. From the 1980s till now, many special functions of smart concrete are derived, including self-test, self-adjustment, self-cleaning, and self-healing [2–5]. The concrete added with new intelligent materials can effectively control crack expansion and even cause cracks to close, so as to improve the service life of the concrete.

Shape Memory Alloys (SMAs), a unique smart material, has been researched and applied more and more in intelligent structures and essential functional components [6–9]. There are two major characteristics simultaneously with the SMAs because of the reversibility of its phase transition. One is the shape memory effect (SME). In the martensite state, applying external force to produce deformation on the SMAs, the deformation will be recovered gradually when the SMAs are heated up to the transformation temperature of the austenite [10]. Depending on the feature above, the SMAs can be used to produce SMA smart concrete, which can improve the mechanical behaviors of concrete members, repair and control the deformation of the structure, and extend its service life.

At present, research of the SMA smart concrete is primarily concentrated on experiments. Numerous results show that concrete structures embedded with SMA wires are effective in

deformation and crack control. Choi's team [11] buried SMA wires after cold drawing in the tensile zone of the reinforced mortar beam and carried out a three-point bend test. And Li et al. [12] buried SMA wires in the reinforced concrete beam. Both of their results showed that the cracks could be closed with a great restoring force generated by heating the built-in SMA wires. Considering the possible complex situations in practical applications, some scholars have studied the related parameters that affect the driving effect of SMA wires and the controlling effect of structural deformation [13, 14]. Many test results show that the quantity, diameter, prestrain, excitation mode, and volume of the SMA wires have a certain influence on the deformation recovery of SMA concrete beam. In addition to the built-in method, SMA wires also can be arranged outside the structure, which has the effect of controlling deformation as well [15–17]. However, due to the complexity of mechanical behaviors of RC structures, there is less numerical analysis than experiment of the SMA concrete structure. Most of them are modeled and analyzed by software of the finite element method (FEM), such as ANSYS, ABAQUS, and SeismoStruct. Based on the superelastic constitutive law of the SMAs, Abdulridha et al. [18] established a finite element (FE) model to simulate the bond interface between SMA wires and concrete with a bond slip element and then obtained the load-displacement relationship of the beam. Khaloo's team [19] used the ANSYS to establish a FE model of a cantilever RC beam embedded with SMA wires. The analysis results showed that, with the increase of the ratio of SMA reinforcement, the shear force and displacement hysteresis curve area of concrete beams decrease; the residual deformation of beams and the cross-sectional stiffness decrease as well. Alam et al. [20] established the FE model of SMA beam-column joints and analyzed its nonlinear behaviors by the SeismoStruct software. Chen and Andrawes [21] carried on the static analysis for the concrete column with SMA wires lateral restraint by the ABAQUS software. When using the FEM to analyze the effect of the SMAs on the structure, it is crucial for the treatment of the SMA recovery force. There are some methods, mainly including pseudo temperature load method [22], negative thermal expansion coefficient method [23], equivalent eccentric force method [24], and equivalent reinforcement stress method [25, 26].

There is no doubt that the FEM is the most widely used numerical method so far, in which the whole structure is discretized with meshes. Due to the dependence of mesh generation, there are some drawbacks such as complicated solution, extensive calculation, and being time consuming for the FEM inevitably [27], while the meshless method can overcome these limitations when analyzing regular structures. In the meshless method, a set of points is used to discretize the solution region and construct approximation functions, which can eliminate meshes completely or partly and need no initiation and repetition of meshes. Thus, the calculation accuracy of the meshless method is ensured and the calculation difficulty is reduced. In the literature [28–30], the mechanical analysis of various structures is performed with different meshless methods, and a series of effective conclusions are obtained. Thereinto, the spline function

method, which is semianalytical and semidiscrete, utilizes spline functions to construct displacement interpolation functions and has a widespread applicability and feasibility in different structural analysis problems. Liu et al. [31] used B-spline finite point method (B-sFPM) to analyze the free transverse vibration of axially functionally graded tapered Euler-Bernoulli beams. Compared with the FEM, the B-sFPM has the advantages of high efficiency and low computational complexity. Based on the B-sFPM, Li et al. [32] proposed the bidirectional B-spline finite point method (BB-sFPM), namely, the spline meshless method, for the parameter identification of piezoelectric laminated plates. This method discretized the structure along two directions with spline nodes, which is more accurate and effective in calculation.

Combining the advantages of the sFPM and the FEM, Professor Qin [33] put forward the unidirectional B-spline QR method (B-sQRM) named after him, which has been successfully implemented in the dynamic, static, and stability analysis of various structures. The B-sQRM is different from the sFPM. In the B-sQRM, one of the directions of the integral structure is discretized by uniformly scattered spline nodes, and the other is discretized by displacement shape functions which can reflect the deformation regularity of the structure. And the structural displacement function is constituted by a linear combination of the product of displacement functions and cubic B-spline functions which are compact and of high order. Moreover, by means of element interpolation functions, element potential energy functions and element stiffness matrices of the FEM, the displacement of element nodes is expressed by the integral displacement of the B-sQRM. Then, the stiffness equation of the entire structure can be established by the total potential energy function and the principle of minimum potential energy. Although the B-spline QR method depends on the discrete mesh and element accuracy of the FEM, the number of unknowns of the B-sQRM is only related to the number of spline nodes and the series of orthogonal polynomials; also it has nothing to do with the number of elements and the total number of node displacements. Therefore, the B-sQRM is of simplicity and convenience in calculation. Based on the above methods, the bidirectional B-spline QR method (BB-sQRM) is proposed in this paper. The principle of the BB-sQRM is the same as the B-sQRM, but the discretization is performed with spline nodes in both two directions of the structure. It has the characteristics of meshless method and can improve the calculation accuracy while the calculation efficiency is guaranteed.

In view of fact that the numerical analysis for nonlinear behaviors of SMA smart concrete beams is less and the employment of the FEM in modeling and analysis is more, therefore, in order to enrich the theoretical system of SMA concrete structures and to increase the diversity of methods, the BB-sQRM is adopted in this paper to perform a nonlinear analysis of the SMA smart concrete beam, which ensures the accuracy of the results while the computational scale is reduced and the efficiency of numerical analysis improved. Based on the classical incremental elastoplastic theory of the RC, the stress-strain relations of elements of concrete and concrete with steel bars under different stress conditions

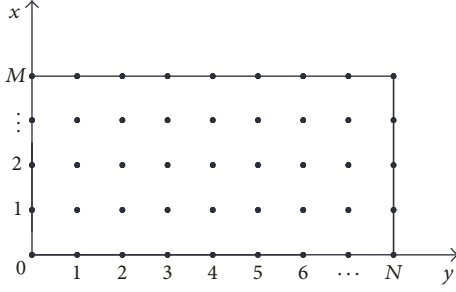


FIGURE 1: Bidirectional spline discretization of plane structure.

are given. By means of the element stiffness matrix of the FEM, the recovery force of SMA wires is equivalent to the eccentric load of spline node by the QR transformation, and the elastoplastic stiffness equation of the RC beam is deduced. Then, based on the iteration method of incremental initial stress, the calculation format for nonlinear analysis of the BB-sQRM is established. The nonlinear behavior such as cracking of the SMA concrete beam can be analyzed by controlling the temperature of SMA wires. Meanwhile, several parameters, such as depth-span ratio, thickness of concrete cover, reinforcement ratio, prestrain, and eccentricity of SMA wires, will be discussed to learn their influence on the capability of crack control, which can provide supplementary and further analytical means for test methods.

2. Principles of the BB-sQRM

In the BB-sQRM, the two directions of the integral structure are discretized by uniformly scattered spline nodes, and the displacement field is constructed by the cubic B-spline functions corresponding to the boundary conditions. The most critical step in the BB-sQRM is the QR transformation presented in Section 2.2. Based on element stiffness matrices, the load vector, and transformed displacement vectors of element nodes, the conversion strategy of total potential energy functions of elements are presented. Thus, the total potential energy function of the entire structure can be obtained directly by adding potential energy functions of elements after the QR transformation. Also, the integration of the total stiffness matrix and the total load vector can be available from the sum of element items in the BB-sQRM, which need not expand before the superposition as the FEM. It means that the solution process is greatly simplified, and the calculation is more efficient and accurate. Moreover, the computer program would be easier to implement. When using the BB-sQRM to analyze nonlinear problems, it just needs to change the expression of element stiffness according to different nonlinear factors and then adjust element values in corresponding positions of the stiffness matrix after materials enter the plastic state.

2.1. Construction of Integral Displacement Function of Structure. As can be seen from Figure 1, the plane structure is discretized along x and y directions. The discrete element is a rectangle element as shown in Figure 2.

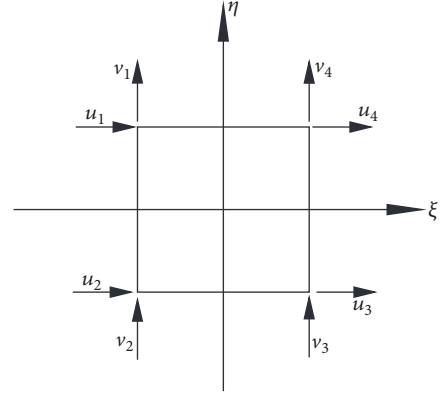


FIGURE 2: Rectangular plane element.

The effect of rotation angle is ignored. The structural displacement field, which is constructed by the linear combination of the product of B-spline functions, can be expressed as follows:

$$\begin{aligned} u &= \sum_{j=0}^M \sum_{i=0}^N u_{ij}^g \phi_i(x) \psi_j(y) = [\psi] \otimes [\phi] \{u^g\}, \\ v &= \sum_{j=0}^M \sum_{i=0}^N v_{ij}^g \phi_i(x) \psi_j(y) = [\psi] \otimes [\phi] \{v^g\}, \end{aligned} \quad (1)$$

where N and M are the maximum numbers of spline nodes in directions of x and y , respectively; $\{u^g\}$ and $\{v^g\}$ are spline generalized displacement arrays; $\phi_i(x)$ and $\psi_j(y)$ are cubic B-spline interpolation basis functions of x and y directions.

Then, (1) can be written in a matrix form, such as

$$\{V\} = [N] \{\delta\}, \quad (2)$$

where $\{V\} = \{u \ v\}^T$ is the displacement array; $[N]$ is the shape function matrix; and $\{\delta\}$ is the generalized displacement array of structural spline nodes; they can be expressed by

$$\begin{aligned} [N] &= \text{diag} [\phi(x) \otimes \psi(y) \ \phi(x) \otimes \psi(y)], \\ [\phi] &= [\phi_0 \ \phi_1 \ \phi_2 \ \cdots \ \phi_{N-1} \ \phi_N], \\ [\psi] &= [\psi_0 \ \psi_1 \ \psi_2 \ \cdots \ \psi_{M-1} \ \psi_M], \\ \{\delta\} &= \{\{\delta\}_0^T \ \{\delta\}_1^T \ \cdots \ \{\delta\}_M^T\}^T, \\ \{\delta_j\} &= \{\{\delta_{0j}\}^T \ \{\delta_{1j}\}^T \ \cdots \ \{\delta_{Nj}\}^T\}^T, \\ \{\delta_{ij}\} &= \{u_{ij}^g \ v_{ij}^g\}^T, \end{aligned} \quad (3)$$

$$\{\delta_j\} = \{\{\delta_{0j}\}^T \ \{\delta_{1j}\}^T \ \cdots \ \{\delta_{Nj}\}^T\}^T, \quad (4)$$

where $i = 0, 1, \dots, N$, $j = 0, 1, \dots, M$. Therefore, the basic unknown $\{\delta\}$ of the BB-sQRM is a vector with order of $2(M+1)(N+1)$.

Based on the displacement parameter method [33], the displacement of spline nodes is taken as the basic unknown.

The basis function $\phi_i(x)$ is constructed by cubic B-spline functions corresponding to boundary conditions, which is expressed by

$$\begin{aligned} \phi_i(x) = & \frac{10}{3}\varphi_3\left(\frac{x-x_0}{h}-i\right) - \frac{4}{3}\varphi_3\left(\frac{x-x_0}{h}-i+\frac{1}{2}\right) \\ & - \frac{4}{3}\varphi_3\left(\frac{x-x_0}{h}-i-\frac{1}{2}\right) \\ & + \frac{1}{6}\varphi_3\left(\frac{x-x_0}{h}-i+1\right) \\ & + \frac{1}{6}\varphi_3\left(\frac{x-x_0}{h}-i-1\right), \end{aligned} \quad (5)$$

where $\varphi_3(x)$ is the cubic B-spline function, which can be seen in [30, 31, 33].

If the spline interpolation basis function $\phi_i(x)$ satisfies the following relation, the boundary problem can be solved easily, and the computation is greatly simplified:

$$\phi_i(x_k) = \begin{cases} 1, & i = k \\ 0, & i \neq k, \end{cases} \quad (6)$$

where x_k denotes the spline nodes of the cubic B-spline function $\varphi_3(x)$; k is the number of spline nodes. Therefrom, $\{u^g\}$ and $\{v^g\}$ obtained by (1) are the real displacements of the structure. Similarly, the spline basis function $\psi_j(y)$ can be constructed.

2.2. QR Transformation. The transformation of the BB-sQRM, which is to establish the conversion relation between the displacement vector of element nodes and the generalized displacement vector of structure spline nodes, is the key step of BB-sQRM.

Using the element stiffness matrix of the FEM and the rectangular element as shown in Figure 2, the displacement vector of element nodes in the overall coordinate system is

$$\{V\}_e = [u_1 \ v_1 \ u_2 \ v_2 \ u_3 \ v_3 \ u_4 \ v_4]^T. \quad (7)$$

According to (1) and (7), the following is presented:

$$\begin{aligned} \{V\}_e &= [[N]_1 \ [N]_2 \ [N]_3 \ [N]_4]^T \begin{bmatrix} \{u^g\} \\ \{v^g\} \end{bmatrix} \\ &= [N]_e \{\delta\}, \end{aligned} \quad (8)$$

where $[N]_e$ is the element shape function matrix; $[N]_m$ ($m = 1, 2, 3, 4$) is the shape function matrix of four nodes of the element, respectively, which can be obtained by substituting the whole coordinate (x_m, y_m) ($m = 1, 2, 3, 4$) of element nodes into (3).

After the QR transformation, the node displacement vector dimension of each element will be expanded to be equal to the node displacement vector dimension of the whole structure; that is, the sixth-order node displacement vector $\{V\}_e$ of elements is to be transformed into a $2(M+1)(N+1)$ -order vector $\{\delta\}$, and it will provide great convenience for subsequent calculation.

3. BB-sQRM Elastoplastic Stiffness Equation of the RC Beam

3.1. The Elastoplastic Increment Constitutive Model of Concrete. The elastoplastic increment constitutive model of concrete is established based on the classical theory of plasticity, which can describe the stress-strain state of the structure in various complex loading processes. And the model has been extensively used in the FEM of concrete materials. Elastoplastic matrices of concrete beam elements in different stress states are given below.

(i) The element elastoplastic matrix of concrete in biaxial compressive stress state is

$$[D]_{ep1} = [D] - [D]_{p1} = [D] ([I] - [Q]_{p1}), \quad (9)$$

where $[D]_{ep1}$ and $[D]_{p1}$ are the concrete elastoplastic matrix and the concrete plastic matrix in the biaxial compressive stress state, respectively; and $[D]$ is the elastic matrix of concrete, which is expressed by

$$[D] = \frac{E}{1-\mu^2} \begin{bmatrix} 1 & \mu & 0 \\ \mu & 1 & 0 \\ 0 & 0 & \frac{1-\mu}{2} \end{bmatrix}, \quad (10)$$

where E is the elastic modulus; μ is the Poisson ratio. $[Q]_{p1}$ is expressed by

$$[Q]_{p1} = \frac{[\partial F/\partial [\sigma]] [\partial F/\partial [\sigma]]^T [D]}{A + [\partial F/\partial [\sigma]]^T [D] [\partial F/\partial [\sigma]]}, \quad (11)$$

where A is the hardening parameter; F is the yield function; element stress $[\sigma] = [\sigma_x \ \sigma_y \ \tau_{xy}]$.

Based on the Chen-Chen yield criterion with 3 parameters [34], using the associated flow law, $[Q]_{p1}$ is expressed by an explicit formulation [35]:

$$\begin{aligned} [Q]_{p1} &= \alpha \begin{bmatrix} a(a+b\mu) & a(b+a\mu) & 18a\tau_{xy}(1-\mu) \\ b(a+b\mu) & b(b+a\mu) & 18b\tau_{xy}(1-\mu) \\ 36\tau_{xy}(a+b\mu) & 36\tau_{xy}(b+a\mu) & 648\tau_{xy}^2(1-\mu) \end{bmatrix} \end{aligned} \quad (12)$$

in which

$$\alpha = \frac{E}{9A(1-\mu^2) - 2Eh},$$

$$a = A_0 + 7\sigma_x - \sigma_y,$$

$$b = A_0 - \sigma_x + 7\sigma_y,$$

$$h = (A_0^2 + 6A_0\sigma_x + 6A_0\sigma_y)(\mu + 1)$$

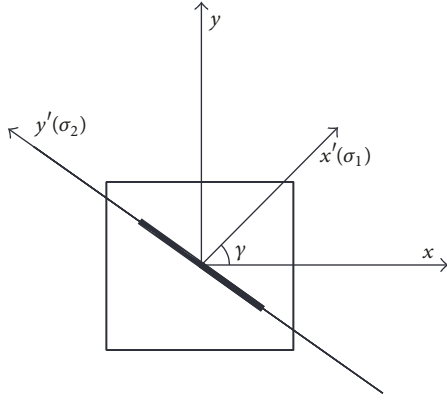


FIGURE 3: Diagram of cracking in the concrete element.

$$\begin{aligned}
 & + (25 - 7\mu) (\sigma_x^2 + \sigma_y^2) + 324\tau_{xy}^2 (1 - \mu) \\
 & + 2\sigma_x\sigma_y (25\mu - 7), \\
 A_0 & = \frac{f_{bc}^2 - f_c^2}{2f_{bc} - f_c}, \\
 A & = \frac{EE_t}{E - E_t},
 \end{aligned} \tag{13}$$

where A_0 is a constant; f_c is the uniaxial compressive strength; f_{bc} is the biaxial compressive strength; E_t is the tangent modulus; E is the elastic modulus; and μ is the Poisson ratio.

Substituting (10) and (13) into (9), the plastic matrix $[D]_{p1}$ and the elastoplastic matrix $[D]_{ep1}$ in the biaxial compressive stress state are obtained. With the proposed explicit expression, the computer programming could be more convenient.

(ii) Under the states of tension-compression stress and biaxial tension stress, the concrete may enter nonlinearity because of cracking. It is assumed that the crack is parallel to the y' axis when the concrete cracks. And the direction of the main tensile stress σ_1 is parallel to the x' axis. As shown in Figure 3, σ_1 and x -axis are with α degree. From x -axis to σ_1 , counterclockwise direction is positive, and clockwise direction is negative.

The elastoplastic matrix of concrete element in the local coordinate system is expressed as $[D^*]_{ep2}$:

$$[D^*]_{ep2} = [D^*] - [D^*]_{p2} = [D^*] ([I] - [Q]_{p2}), \tag{14}$$

in which

$$[Q]_{p2} = \begin{bmatrix} 0 & 0 & 0 \\ \nu & 1 & 0 \\ 0 & 0 & 1 - \beta \end{bmatrix}, \tag{15}$$

where β is the residual shear coefficient, whose value is 0.5 in the ordinary RC beam.

The element elastoplastic matrix $[D]_{ep2}$ of the two stress states in the whole coordinate system is obtained by the transformation:

$$[D]_{ep2} = [T]^T [D^*]_{ep} [T], \tag{16}$$

where $[T]$ is the coordinate transformation matrix, which is expressed by

$$[T] = \begin{bmatrix} c^2 & s^2 & c \times s \\ s^2 & c^2 & -c \times s \\ -2c \times s & 2c \times s & c^2 - s^2 \end{bmatrix}, \tag{17}$$

where $c = \cos \gamma$, $s = \sin \gamma$; γ is the angle between the x' axis of the local coordinate and the x -axis of the whole coordinate in Figure 3.

Also, the plastic matrix of concrete element of the two stress states is obtained by

$$[D]_{p2} = [T]^T [D^*]_{p2} [T], \tag{18}$$

in which

$$[D^*]_{p2} = [D^*] [Q]_{p2}, \tag{19}$$

where $[D^*]_{p2}$ is the plastic matrix in the local coordinate system; and $[D^*]$ is the same as (11).

Substituting (10), (14), (15), and (17) into (16), the elastoplastic matrix $[D]_{ep2}$ is obtained. And the plastic matrix $[D]_{p2}$ is obtained by substituting (10), (17), and (19) into (18).

3.2. Additional Stress and Release Stress. The plastic deformation of the concrete element subjected to the biaxial compression could create the additional stress $\{\sigma_0\}$, which is obtained by

$$\{\sigma_0\} = [D]_{p1} \{\varepsilon\}, \tag{20}$$

where $\{\varepsilon\}$ is the strain of the concrete element.

The crack of the concrete element subjected to the biaxial tension and tension-compression could create the release stress $\{\sigma_R\}$, which is obtained by

$$\{\sigma_R\} = [I] - \{p(\gamma)\} \{q(\gamma)\}^T \begin{Bmatrix} \sigma_x \\ \sigma_y \\ \tau_{xy} \end{Bmatrix}, \tag{21}$$

in which

$$\begin{aligned}
 \{p(\gamma)\} & = [\sin^2 \gamma \quad \cos^2 \gamma \quad \sin \gamma \cos \gamma]^T, \\
 \{q(\gamma)\} & = [\sin^2 \gamma \quad \cos^2 \gamma \quad 2 \sin \gamma \cos \gamma]^T,
 \end{aligned} \tag{22}$$

where γ is the angle between the σ_1 axis of the local coordinate and the x -axis of the whole coordinate as shown in Figure 3.

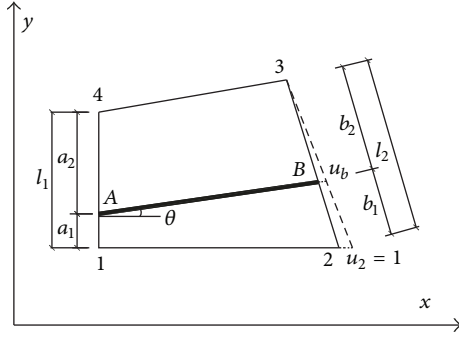


FIGURE 4: Quadrilateral reinforced concrete composite element.

3.3. Elastoplastic Stiffness Equation of Reinforced Concrete Beam Based on BB-sQRM. There are mainly three kinds of FE models which can be chosen to analyze RC structures: integrated, separated, and combined [36]. In this paper, the combined model is adopted. The plain concrete element and the reinforced concrete element are created after the spline discretization. The contribution of concrete and steel bars to the stiffness should be considered simultaneously when the stiffness matrix element is established.

The element stiffness matrix of the plain concrete $[K_c]_e$ can be expressed by

$$[K_c]_e = \int_{-1}^{+1} \int_{-1}^{+1} [B]_e^T [D] [B]_e^T |J| t d\xi d\eta, \quad (23)$$

where $[B]_e$ is the element strain matrix; $[D]$ is the elastic matrix of concrete; $|J|$ is the Jacobian determinant; ξ and η are of the local coordinate.

The element with steel bars is simulated by a four-node composite element as shown in Figure 4. The element stiffness matrix of the steel bar $[K_s]_e$, which is the contribution matrix of the steel bar to the whole quadrilateral element, is formed by the element stiffness matrix of the single steel bar $[\bar{K}_s]_e$:

$$[K_s]_e = [R]^T [\bar{K}_s]_e [R], \quad (24)$$

where $[R]$ is a coordinate transformation matrix expressed by

$$[R] = \begin{bmatrix} \frac{a_1}{l_1} & 0 & 0 & 0 & 0 & 0 & \frac{a_2}{l_1} & 0 \\ 0 & \frac{a_1}{l_1} & 0 & 0 & 0 & 0 & 0 & \frac{a_2}{l_1} \\ 0 & 0 & \frac{b_1}{l_2} & 0 & \frac{b_2}{l_2} & 0 & 0 & 0 \\ 0 & 0 & 0 & \frac{b_1}{l_2} & 0 & \frac{b_2}{l_2} & 0 & 0 \end{bmatrix}, \quad (25)$$

where $a_1, a_2, b_1, b_2, l_1,$ and l_2 are the lengths shown in Figure 4.

It is assumed that the length of a steel bar element is l , and the angle between the steel bar and x -axis is θ . $c' = \cos \theta$,

$s' = \sin \theta$. Then the element stiffness matrix of the single steel bar is obtained by

$$[\bar{K}_s]_e = \frac{EA}{l} \begin{bmatrix} c'^2 & c's' & -c'^2 & -c's' \\ c's' & s'^2 & -c's' & -s'^2 \\ -c'^2 & -c's' & c'^2 & c's' \\ -c's' & -s'^2 & c's' & s'^2 \end{bmatrix}. \quad (26)$$

The stiffness matrix of reinforced concrete composite element $[K_{sc}]_e$ can be obtained by the superposition of the element stiffness matrix of steel bars $[K_s]_e$ and the element stiffness matrix of the plain concrete $[K_c]_e$:

$$[K_{sc}]_e = [K_c]_e + [K_s]_e. \quad (27)$$

Then, the general potential energy functions of the reinforced concrete composite element and the plain concrete element are expressed by the following:

$$\begin{aligned} \Pi_k^e &= \frac{1}{2} \{V_{sc}\}_e^T [K_{sc}]_e \{V_{sc}\}_e \\ &\quad - \{V_{sc}\}_e^T (\{f_{sc}\}_e + \{f_{sc}^P\}_e + \{f_{sc}^R\}_e), \end{aligned} \quad (28)$$

$$\begin{aligned} \Pi_k^e &= \frac{1}{2} \{V_c\}_e^T [K_c]_e \{V_c\}_e \\ &\quad - \{V_c\}_e^T (\{f_c\}_e + \{f_c^P\}_e + \{f_c^R\}_e), \end{aligned}$$

where $\{f_{sc}\}_e$ and $\{f_c\}_e$ are the node force vectors of elements; $\{f_{sc}^P\}_e$ and $\{f_c^P\}_e$ are the additional node force vectors of elements; $\{f_{sc}^R\}_e$ and $\{f_c^R\}_e$ are the node force vectors of cracking elements:

$$\begin{aligned} \{f_k^P\}_e &= \int_e [B]_e^T \{\sigma_0\} d\Omega, \\ \{f_k^R\}_e &= \int_e [B]_e^T \{\sigma_R\} d\Omega, \end{aligned} \quad (29)$$

where the corner "k" represents the composite element (sc) or the plain concrete element (c); and $[B]_e$ is the element strain matrix; $\{\sigma_0\}$ and $\{\sigma_R\}$ are obtained by (20) and (21).

After the QR transformation, the general potential energy function of element, which is expressed by the generalized displacement vector of spline nodes can be presented:

$$\Pi_e = \frac{1}{2} \{\delta\}^T [G]_e \{\delta\} - \{\delta\}^T (\{F\}_e + \{F^P\}_e + \{F^R\}_e), \quad (30)$$

in which

$$\begin{aligned} [K]_e &= [N]_e^T [K_{sc}]_e [N]_e + [N]_e^T [K_c]_e 0 [N]_e, \\ \{F\}_e &= [N]_e^T \{f_{sc}\}_e + [N]_e^T \{f_c\}_e, \\ \{F^P\}_e &= [N]_e^T \{f_{sc}^P\}_e + [N]_e^T \{f_c^P\}_e, \\ \{F^R\}_e &= [N]_e^T \{f_{sc}^R\}_e + [N]_e^T \{f_c^R\}_e, \end{aligned} \quad (31)$$

where $[K]_e$ is the element general stiffness matrix; $\{F\}_e$ is the element load vector; $\{F^P\}_e$ is the element additional load

vector created by the plastic deformation; $\{F^R\}_e$ is the load vector transformed by release stress of the cracking elements.

If the concrete beam is divided into n elements, its general potential energy function can be expressed by

$$\Pi = \frac{1}{2} \{\delta\}^T [K] \{\delta\} - \{\delta\}^T (\{F\} + \{F^P\} + \{F^R\}) \quad (32)$$

in which

$$\begin{aligned} [K] &= \sum_{e=1}^n [G]_e, \\ [F] &= \sum_{e=1}^n \{F\}_e, \\ [F^P] &= \sum_{e=1}^n \{F^P\}_e, \\ [F^R] &= \sum_{e=1}^n \{F^R\}_e. \end{aligned} \quad (33)$$

So, it is quite easy and convenient to establish the general stiffness matrix and the general load vector with the superposition of element stiffness matrices and element load vectors by using the BB-sQRM. According to the principle of minimum potential energy, the elastoplastic stiffness equation of the RC beam can be obtained by (32):

$$[K] \{\delta\} = \{F\} + \{F^P\} + \{F^R\}. \quad (34)$$

Then, the displacement vector and the stress vector can be obtained by

$$\begin{aligned} \{\delta\} &= [K]^{-1} (\{F\} + \{F^P\} + \{F^R\}), \\ \{\sigma\} &= [D]_{ep} [B] [N]_e \{\delta\}, \end{aligned} \quad (35)$$

where the elastoplastic matrix $[D]_{ep}$ is obtained by (9) or (16).

3.4. The Solution Process of the BB-sQRM Elastoplastic Stiffness Equation. In this paper, the incremental iteration method for initial stress is adopted to solve the elastoplastic stiffness equation. Here are the steps.

(1) Divide the external load into N stages. The initial displacement $\{\delta\}_0 = 0$, and the initial stress $\{\sigma\}_0 = 0$.

(2) Apply the first stage load $\{F\}_1$, which usually takes 10% to 30% of the predicted limit load. Make the displacement increment norm of the first iteration zero. Then the structure is in an elastic state at present. According to the elastic stiffness matrix $[K]_1$, calculate the increment of the structure displacement:

$$\{d\delta\}_1 = [K]_1^{-1} \{F\}_1. \quad (36)$$

(3) According to the geometric equation, calculate the increment of the element strain $\{d\varepsilon\}_1$; and according to the elastic stress-strain relationship, the increment of the element stress $\{d\sigma\}_1$ can be obtained by

$$\{d\sigma\}_1 = [D] [B]_e [N]_e \{d\delta\}_1. \quad (37)$$

Then the element stress components σ_x, σ_y , and τ_{xy} under first stage load can be derived. Also, the main stresses σ_1 and σ_2 under this stage load can be obtained.

(4) Determine the stress state of each element on the basis of σ_1 and σ_2 .

If the element is under the state of biaxial compression stress, calculate the element elastoplastic matrix $[D]_{ep1}$ and the plastic matrix $[D]_{p1}$ by (9), (10), and (12); and calculate the additional node force vector $\{f_k^P\}_e$ by (20) and (29).

If the elements are subjected to the tension-compression stress or the biaxial tension stress, calculate the element elastoplastic matrix $[D]_{ep2}$ and the plastic matrix $[D]_{p2}$ by (14)–(19); and calculate the node force vectors of cracking elements $\{f_k^R\}_e$ by (21), (22), and (29).

Then transform the obtained matrices and vectors above into the corresponding matrices and vectors of the BB-sQRM.

(5) After processing all the elements by step (4), the load increment array under current iteration can be obtained by (29), (31), and (33):

$$\{dF\}_1 = \{dF^P\} + \{dF^R\}. \quad (38)$$

Then calculate the new general stiffness matrix $[K]$ and new displacement increment.

(6) Determine whether the iteration converges.

If the norm of the displacement increment satisfies the criterion of iteration convergence, the iterative computation of the load on the current stage is stopped and then enters the next step:

$$\|\{d\delta\}_1^j\| < 10^{-8}, \quad (39)$$

where the corner “ j ” represents the number of iterations after increasing each load increment.

If the condition above is not satisfied, repeat steps (4)–(6) on the basis of the stress increment obtained by the new displacement increment.

(7) With the element state after finishing the first load calculation as the initial state, apply the second stage load. Calculate the displacement increment of the second load:

$$\{d\delta\}_2 = [K]_2^{-1} \{F\}_2. \quad (40)$$

Then the stress increment can be obtained. Repeat steps (3)–(6), until the second load iteration finishes.

(8) Apply the load progressively to number N load, and complete the solution.

4. Crack Control Effect Analysis of SMA Smart Concrete Beam

4.1. The Stiffness Equation of the SMA Concrete Beam Based on BB-sQRM. The introduction of the SMA driving force is one of the key steps while establishing the crack equation of the SMA concrete beam. In this paper, the SMA recovery force is simulated by the equivalent eccentric force method. That is, the SMA wires are not processed into elements in the bidirection spline discretization of the structure. Instead, the recovery force of SMA wires is equivalent to the eccentric

TABLE 1: The recovery stress σ^r in a certain temperature range of SMA wires with different prestrains (MPa).

Temperature ($^{\circ}\text{C}$)	Stress of 4% prestrain	Stress of 6% prestrain	Stress of 8% prestrain
20	0	0	0
30	2.714	2.731	2.748
40	7.412	9.543	13.647
50	62.341	39.423	27.481
60	165.834	197.854	112.572
70	218.125	275.371	158.407
80	241.534	309.025	339.418
90	281.413	365.412	394.857
100	296.417	379.142	501.637
110	325.426	395.427	537.486
120	327.013	399.652	595.213

force, which is introduced in Section 4.2. The spline node load $\{f_{\text{SMA}}\}$ based on BB-sQRM is transformed by the driving force of SMA wires:

$$\{f_{\text{SMA}}\} = [N]_i \begin{Bmatrix} T_{\text{SMA}} \\ 0 \end{Bmatrix}, \quad (41)$$

where the SMA driving force T_{SMA} , which is produced by the electric excitation, can be obtained by the equivalent eccentric force method.

Adding $\{f_{\text{SMA}}\}$ into (28), the general potential energy function of the concrete composite element with SMA wires can be obtained. Then repeat the calculations from (24) to (34). According to the QR transformation and element discretization, the stiffness equation of the SMA concrete beam is derived by the principle of minimum potential energy and the BB-sQRM:

$$[K] \{\delta\} = \{F\} + \{F^p\} + \{F^R\} + \{F_{\text{SMA}}\}, \quad (42)$$

in which

$$\{F_{\text{SMA}}\} = \sum_{e=1}^n [N]_e^T \begin{Bmatrix} T_{\text{SMA}} \\ 0 \end{Bmatrix}. \quad (43)$$

When cracks of concrete beam are produced under the load, stimulate the SMA wires which are buried in the beam with electric currents. Then the phase transition of SMA wires occurs and the recovery stress is produced. And the driving force vector $\{F_{\text{SMA}}\}$ is formed, which can control cracks development. Therefore, in order to obtain the elastoplastic stiffness equation of the SMA smart concrete beam, the driving force of SMA wires should be added to the last step in Section 3.4. That is, ‘‘apply the load progressively to the no. N load, and apply the driving force of SMA wires, then complete the solution.’’ Thus, the displacement of the structure and the maximum stress and strain of the steel bar elements can be obtained by the proposed model, and the maximum crack width of the concrete beam can be calculated.

The maximum crack width of the concrete beam is obtained by the following:

$$\omega_{\text{max}} = \alpha_{\text{cr}} \varphi \varepsilon_{\text{max}} L, \quad (44)$$

where L is the length of the steel bar elements; α_{cr} and φ are determined by [37].

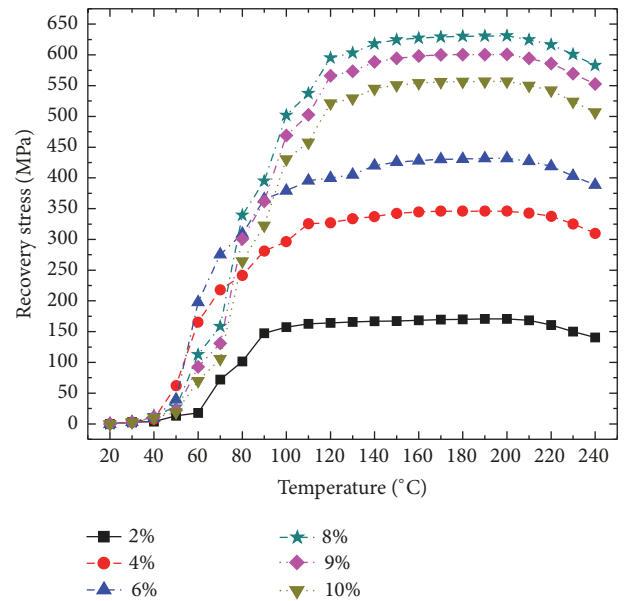


FIGURE 5: The recovery stress-temperature curves of SMA with different prestrains.

4.2. *Test and Simulation Method of SMA Recovery Stress.* In order to learn the driving characteristics of SMA wires in the electric excitation, the recovery stress test of SMA wires was carried out [25]. SMA materials used were Ni-Ti wires, where the Ni accounted for 44.24% and Ti accounted for 55.76%. The original length was 300 mm, and diameter was 2 mm. The maximum recovery stress was 680 MPa, and the maximum recovery strain was 8%. The constant electric current was determined to be adopted in the next test; recovery stress-temperature curves of SMA wires in different prestrains from 2% to 10% were measured. The curves are shown in Figure 5. The recovery stress values in a certain temperature range of SMA wires with 4%, 6%, and 8% prestrains are shown in Table 1.

As shown in Figure 6 and Table 1, when the prestrain is identical, with the rise of temperature, the austenite transformation occurs, and the recovery stress of SMA wires

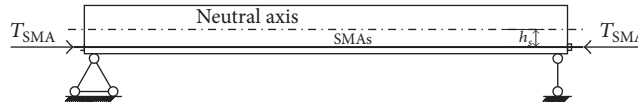


FIGURE 6: The equivalent eccentric force of SMA wires.

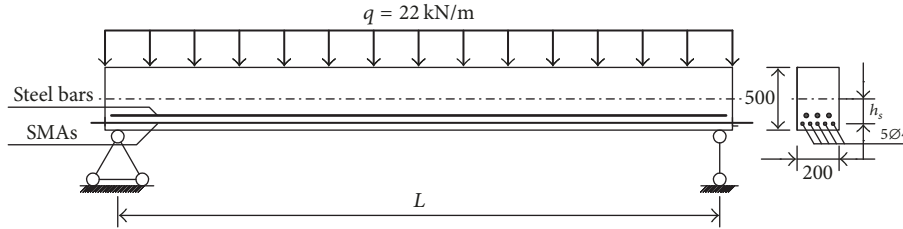


FIGURE 7: The simply supported reinforced concrete beam.

increases. The stress tends to be stable at 120°C. After heating up to 200°C, SMA wires soften and lose shape memory effect gradually. When the prestrain of SMA wires is not greater than 8%, the maximum recovery stress of SMA wires increases with the increasement of the prestrains. Conversely, after more than 8%, the maximum recovery stress of SMA wires decreases with the rise of prestrains.

The recovery stress of SMA wires can be processed based on a set of related test data. The methods for simulating the recovery force of SMA wires are mainly divided into two categories. One relates to thermodynamic analysis, which needs to define the elastic modulus at different temperatures during the application of temperature, such as the pseudo temperature loading method and negative thermal strain method. The other is applying the recovery force as the external load on the structure, such as the equivalent eccentric force method and the equivalent steel bar stress method. In this paper, the equivalent eccentric force method is adopted. This method, which does not involve the complex thermal behavior in the analysis process, is more convenient to realize in model establishment and computer programming.

Based on the equivalent eccentric force method, the recovery force of SMA wires is equivalent to a pair of horizontal forces, which are applied to both ends of the concrete beam, as shown in Figure 7. According to the arrangement of longitudinal steel bars, the SMA wires are embedded and anchored in the tension zone at the bottom of the concrete beam. When SMA wires are heated, the phase transformation and the contraction of SMA wires occur. Because of the constraint of the anchorages, the contraction of SMA wires is limited. And the eccentric driving force is formed and applied at the bottom of the concrete beam. Therefore, the active control of the structure deformation and the crack control can be realized.

The equivalent horizontal force T_{SMA} and the bending moment M_{SMA} of SMA wires can be obtained by

$$\begin{aligned} T_{SMA} &= n\sigma^r A_{SMA}, \\ M_{SMA} &= T_{SMA}h_s, \end{aligned} \quad (45)$$

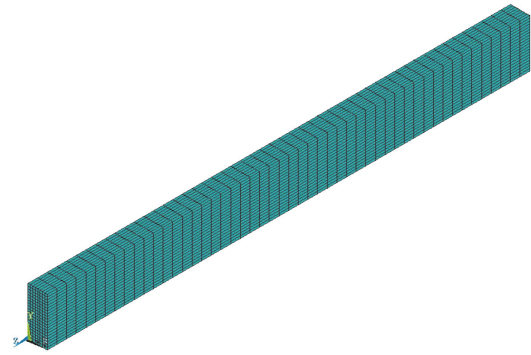


FIGURE 8: FE model of the SMA reinforced concrete beam.

where n is the number of SMA wires; σ^r is the recovery stress of SMA wires in Table 1; A_{SMA} is the cross-sectional area of single SMA wire; h_s is the distance from SMA wires to the neutral axis of the concrete beam, that is, the eccentricity of SMA wires. In ANSYS, the recovery force of SMA wires is equivalent to the horizontal eccentric force, which is applied on the concrete beam model as the external load. Therefore, the finite element (FE) simulation of the concrete crack control with SMA wires can be realized.

5. Result and Discussion

In this paper, the crack control effect of a simply supported RC beam embedded with SMA wires is considered. Through the numerical example, the correctness of the proposed BB-SQRm can be verified. Also, a discussion for the influence of several parameters on crack control effect is presented in the example. The basic RC beam model is shown in Figure 8. The cross section is $b \times h = 200 \text{ mm} \times 500 \text{ mm}$, and the calculated span is expressed in L . The uniformly distributed load is $q = 22 \text{ kN/m}$ and the C25 concrete is adopted. The tension zone is embedded with three HRB400 steel bars and five SMA wires where the diameter is 4 mm. The relevant parameters are $E_C = 2.55 \times 10^4 \text{ N/mm}^2$, $E_s = 2 \times 10^5 \text{ N/mm}^2$, $f_{ck} = 16.7 \text{ N/mm}^2$, and $f_{tk} = 1.78 \text{ N/mm}^2$. The recovery stress of

TABLE 2: Designation and parameters of SMA reinforced concrete beams.

Designation	Beam dimension (mm)	Concrete cover (mm)	Reinforcement ratios (%)	Prestrain of SMA wires (%)	Eccentric distances of SMA wires (mm)
B1	200 × 500 × 4000	25	0.76	6	220
B2	200 × 500 × 5000	25	0.76	6	220
B3	200 × 500 × 6000	25	0.76	6	220
B4	200 × 500 × 5000	45	0.76	6	220
B5	200 × 500 × 5000	65	0.76	6	220
B6	200 × 500 × 5000	25	0.46	6	220
B7	200 × 500 × 5000	25	1.14	6	220
B8	200 × 500 × 5000	25	0.76	4	220
B9	200 × 500 × 5000	25	0.76	8	220
B10	200 × 500 × 5000	25	0.76	6	110
B11	200 × 500 × 5000	25	0.76	6	160

Note. B1, B2, and B3 are different in depth-span ratios; B2, B4, and B5 are different in concrete cover; B2, B6, and B7 are different in reinforcement ratios; B2, B8, and B9 are different in prestrain of SMA wires; B2, B10, and B11 are different in eccentric distances of SMA wires.

SMA wires comes from the test data shown in Table 1, and its simulation employs the equivalent eccentric force method introduced in Section 4.2. Based on the basic model shown in Figure 8, the different beam models are designed according to several parameters, which are listed in Table 2.

5.1. Comparison of the Results of BB-sQRM and FEM in ANSYS. A comparison example of the two methods is presented, which is to verify the correctness of the proposed crack control analysis model based on BB-sQRM. Beam 2 (B2) in Table 2 is used as the SMA reinforced concrete model for this numerical example. In order to obtain the maximum crack width of the SMA concrete beam in different temperatures, both ANSYS and BB-sQRM need to be used in calculating the maximum strain of steel bar elements. The final result can be calculated by (44). Consequently, the obtained maximum strain of steel bars is utilized to compare in the verification process. First, use the ANSYS in finite element analysis. Both the SOLID65 elements and the LINK 180 elements are adopted in modeling. When dividing the mesh, considering the equivalent load of SMA wires need to be applied on the node, the width direction of the concrete beam is divided into 6 equal parts. And one mesh is increased along the height direction based on 25 equal parts. That is, the mesh generation of the concrete beam is, namely, $50 \times 26 \times 6$, in which the number of elements is 10550, the number of nodes is 12393, and the total number of the degrees of freedom is 74313. The model of FEM is shown in Figure 9. Second, based on BB-sQRM, a plane model shown in Figure 1 is used for analysis. The spline node discretization of 50×25 has 1250 elements, 1326 nodes, and 3975 degrees of freedom. Meanwhile, in order to discuss the effect of spline node discretization on the precision of calculation and check the convergence of the BB-sQRM, the maximum strain in other discrete cases has also been calculated. The numerical results are listed in Table 3. The maximum strain error of steel bars obtained by comparing the two methods under different

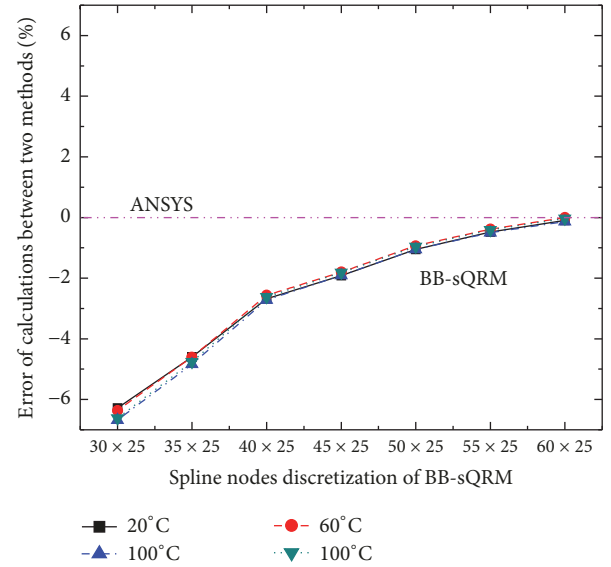


FIGURE 9: Convergence efficiency of the BB-sQRM.

discretization is shown in Figure 10. And the convergence efficiency of the BB-sQRM in different discretization is illustrated in Figure 11.

As shown in Table 3 and Figure 10, the more the number of spline nodes is, the closer the results between ANSYS and BB-sQRM are. When the discretization is 30×25 , 35×25 , 40×25 , 45×25 , 50×25 , 55×25 , and 60×25 , respectively, the maximum error is -6.68% , -4.84% , -2.71% , -1.92% , -1.06% , -0.51% , and -0.13% , which converges quickly. As shown in Figure 11, under different SMA temperatures of 20°C , 60°C , and 120°C , with the spline node discretization from 30×25 to 60×25 , the maximum strain of steel bar elements is stabilized gradually. However, as far as the total degrees of freedom are

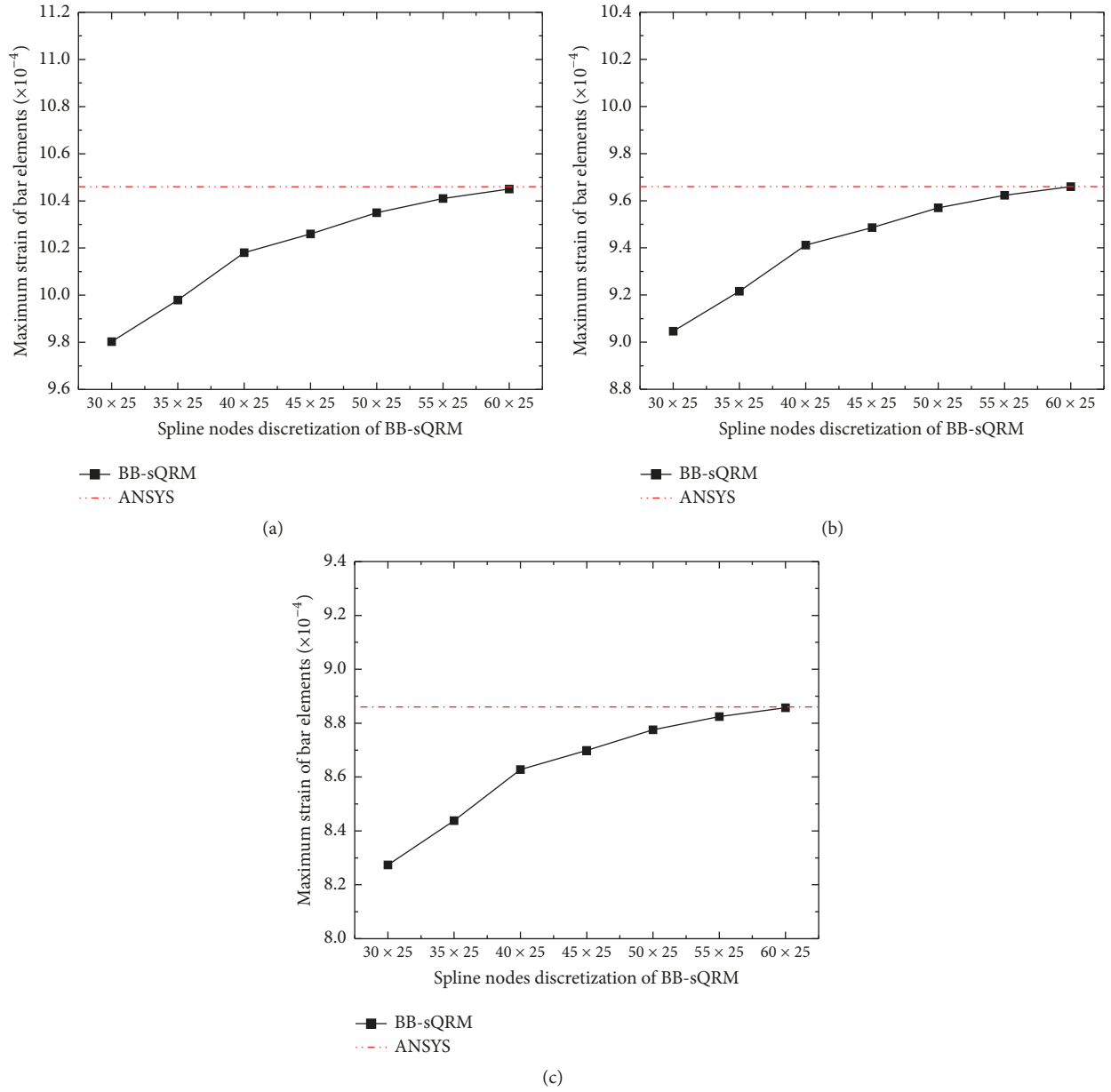


FIGURE 10: Maximum strain of bar steel elements with respect to spline notes discretization: (a) 20°C, (b) 60°C, and (c) 120°C.

TABLE 3: Maximum strain of steel bar elements with different discretization and temperatures ($\times 10^{-4}$).

Method	Discretization	Temperature ($^{\circ}\text{C}$)					
		20	40	60	80	100	120
BB-sQRM	30 \times 25	9.803	9.766	9.046	8.620	8.352	8.274
	35 \times 25	9.979	9.943	9.216	8.788	8.517	8.438
	40 \times 25	10.180	10.140	9.412	8.980	8.707	8.628
	45 \times 25	10.260	10.220	9.486	9.053	8.779	8.699
	50 \times 25	10.350	10.310	9.570	9.132	8.856	8.775
	55 \times 25	10.410	10.370	9.623	9.183	8.905	8.824
	60 \times 25	10.450	10.410	9.660	9.218	8.938	8.857
ANSYS	50 \times 26 \times 6	10.460	10.420	9.660	9.230	8.950	8.860

TABLE 4: The recovery situation of maximum crack width with different depth-span ratios.

Temperature of SMA wires (°C)	Maximum crack width (mm)			Recovery rate of maximum crack width (%)		
	ζ_1	ζ_2	ζ_3	ζ_1	ζ_2	ζ_3
20	0.1002	0.2098	0.3500	0.00	0.00	0.00
40	0.0996	0.2090	0.3491	0.59	0.39	0.27
60	0.0886	0.1940	0.3315	11.61	7.54	5.29
80	0.0821	0.1851	0.3211	18.10	11.77	8.26
100	0.0780	0.1795	0.3146	22.20	14.44	10.11
120	0.0768	0.1779	0.3128	23.40	15.22	10.64

Depth-span ratios (ζ): $\zeta_1 = h_1/L_1 = 1:8$, $\zeta_2 = h_2/L_2 = 1:10$, and $\zeta_3 = h_3/L_3 = 1:12$.

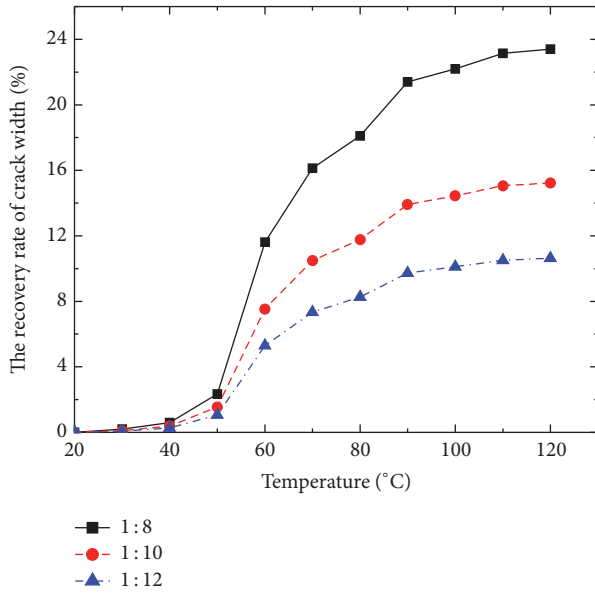


FIGURE 11: The recovery rates of maximum crack width with different depth-span ratios of the beams.

concerned, the computation of the BB-sQRM is much less than that of the FEM.

The main reasons for the error between the BB-sQRM and the FEM are as follows: (1) The type of elements used in the two methods is different. The plane stress elements were utilized in the BB-sQRM, while the three-dimensional solid elements were adopted in the ANSYS differently. Thus, the degrees of freedom of nodes are distinguishing. (2) The material constitutive law used in the two methods is different. The BB-sQRM was applied to different stress zone of reinforced concrete beam with different yield criteria and failure criteria. In the FEM analysis by ANSYS, the same stress-strain relationship was assumed for all stress zones. Therefore, the above-mentioned errors of the two methods are permissible and reasonable, and the model of the SMA concrete beam based on the BB-sQRM is correct and effective.

5.2. Parameter Analysis. Based on the above verification, using the BB-sQRM elastoplastic analysis program of the SMA smart concrete beam with the crack control property, the maximum crack width can be calculated and the influence

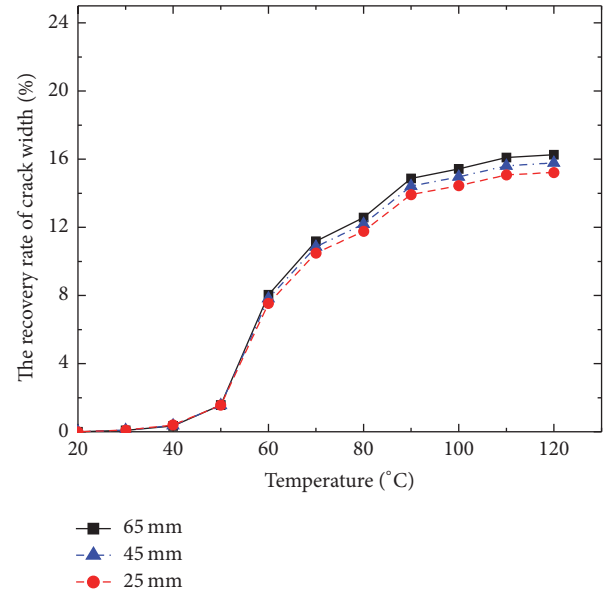


FIGURE 12: The recovery rates of maximum crack width with different thickness of concrete cover.

on the crack control effect of different parameters can be discussed. In this paper, depth-span ratio, thickness of concrete cover, reinforcement ratio of concrete beams, and prestrain and eccentricity of SMA wires are selected as the parameters. Utilizing the recovery stress-temperature curve of SMA wires measured by test, the nonlinear analysis and the crack control analysis of the SMA concrete beam under different working conditions are carried out. The various parameter models are shown in Table 2. The materials of the reinforced concrete beam, the cross section, and the load are unchanged. The example is calculated by the BB-sQRM with the discretization of 50×25 .

5.2.1. Effect of Depth-Span Ratios. The effect of crack control on SMA reinforced concrete beam under different depth-span ratios is considered by using the models B1, B2, and B3. The height of the cross section remained, and the calculated span of the beams is 4 m, 5 m, and 6 m, respectively. As shown in Table 4 and Figure 12, when the SMA is in the normal temperature (20°C), the maximum crack width is 0.1002 mm, 0.2098 mm, and 0.3500 mm severally. After the

TABLE 5: The recovery situation of maximum crack width with different thickness of concrete cover.

Temperature of SMA wires (°C)	Maximum crack width (mm)			Recovery rate of maximum crack width (%)		
	\bar{c}_1	\bar{c}_2	\bar{c}_3	\bar{c}_1	\bar{c}_2	\bar{c}_3
20	0.2098	0.2848	0.3700	0.00	0.00	0.00
40	0.2090	0.2838	0.3687	0.39	0.37	0.34
60	0.1940	0.2625	0.3403	7.54	7.82	8.04
80	0.1851	0.2501	0.3234	11.77	12.19	12.58
100	0.1795	0.2422	0.3129	14.44	14.97	15.43
120	0.1779	0.2399	0.3098	15.22	15.78	16.26

Concrete covers (\bar{c}): $\bar{c}_1 = 25$ mm, $\bar{c}_2 = 45$ mm, and $\bar{c}_3 = 65$ mm.

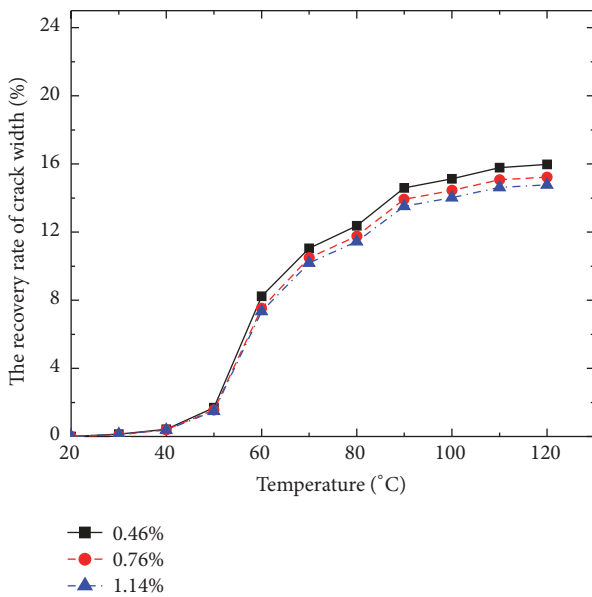


FIGURE 13: The recovery rates of maximum crack width with different reinforcement ratios.

SMA wires are heat-treated into 120°C, the recovery rate of the maximum crack width reached 23.40%, 15.22%, and 10.64%. Significantly, with the depth-span ratios reduction, the beam is more slender, and the initial maximum crack width of the beam without heating of SMA wires increases, but the recovery rate of the maximum crack width decreases significantly, which indicates that the depth-span ratio has a considerable influence on the crack control effect. The reason is that when cracks are driven to control by SMA wires, the higher the depth-span ratio is, the greater the eccentric moment formed by the recovery force of SMA wires is, and the better the driving effect is. Conversely, the lower the depth-span ratio is, the greater the beam deformation is, and the weaker the driving effect of SMA wires is.

5.2.2. *Effect of the Thickness of the Concrete Cover.* Depending on the specification of the design of reinforced concrete beam, the concrete cover affects the development of the beam cracks significantly. As shown in Table 5 and Figure 13, when the thickness of the concrete cover is 25 mm (in B2), 45 mm (in B4), and 65 mm (in B5), the maximum crack width

of the beam before heat-treating is 0.2098 mm, 0.2848 mm, and 0.3700 mm, respectively. And the recovery rate of the maximum crack achieves 15.22%, 15.78%, and 16.26% after heating the SMA wires to 120°C. Thus, with the increasing of the thickness of the concrete cover, the recovery rate of the maximum crack width increases. However, the increment of the recovery-temperature curve is very small with the same thickness of the concrete cover, because, for the reinforced concrete beam, increasing the thickness of concrete cover can make the crack develop more fully. Then the prestrain of the SMA wires increases accordingly, and the recovery stress is greater after heating the SMA wires with electric excitation. So it is useful for control crack by increasing the concrete cover thickness, though the effect is not evident.

5.2.3. *Effect of the Reinforcement Ratios in Tension Zone.* In order to check the influence on the crack control effect of the reinforcement ratios, the models of B6, B2, and B7 are used. With the same number of SMA wires embedded in the concrete beam, make the reinforcement ratios 0.46%, 0.76%, and 1.14%, respectively. That is, 3 steel bars of HRB400 in different diameters of 14 mm, 18 mm, and 22 mm are embedded in the tension zone. The calculated results are shown in Table 6 and Figure 14. In the normal temperature, the maximum crack width of the reinforced concrete beam is 0.3935 mm, 0.2098 mm, and 0.1275 mm. Heating the SMA wires to 120°C, the recovery rate of the maximum crack width is 15.97%, 15.22%, and 14.78%, respectively. The results illustrate that the larger the reinforcement ratio is, the worse the property of the crack control on the SMA concrete beam is. In respect that the plastic deformation of steel bars and the bond degrees of concrete both hinder the recovery of cracks and deformation, which make the driving effect of SMA wires weak, the hindering effect becomes obvious with the increment of the reinforcement ratio.

5.2.4. *Effect of the Prestrain of SMA Wires.* The prestrain of SMA wires in models B8, B2, and B9 is 4%, 6%, and 8%, respectively. The SMA wires are heat-treated to the temperature of the maximum recovery stress, and the result is illustrated in Figure 15. The prestrain of the three models is 0.2098 mm. When the exciting temperature is 180°C, the maximum crack width of the concrete beam is 0.1822 mm, 0.1754 mm, and 0.1595 mm, and the recovery is correspondingly 13.17%, 16.41%, and 24.0%. Obviously, with the increase

TABLE 6: The recovery situation of maximum crack width with different reinforcement ratios.

Temperature of SMA wires (°C)	Maximum crack width (mm)			Recovery rate of maximum crack width (%)		
	α_{s1}	α_{s2}	α_{s3}	α_{s1}	α_{s2}	α_{s3}
20	0.3935	0.2098	0.1275	0.00	0.00	0.00
40	0.3918	0.2090	0.1270	0.43	0.39	0.38
60	0.3611	0.1940	0.1181	8.23	7.54	7.34
80	0.3448	0.1851	0.1129	12.37	11.77	11.44
100	0.3340	0.1795	0.1096	15.13	14.44	14.02
120	0.3307	0.1779	0.1087	15.97	15.22	14.78

Reinforcement ratios (α_s): $\alpha_{s1} = 0.46\%$ (reinforcement diameter 14 mm), $\alpha_{s2} = 0.76\%$ (reinforcement diameter 18 mm), and $\alpha_{s3} = 1.14\%$ (reinforcement diameter 22 mm).

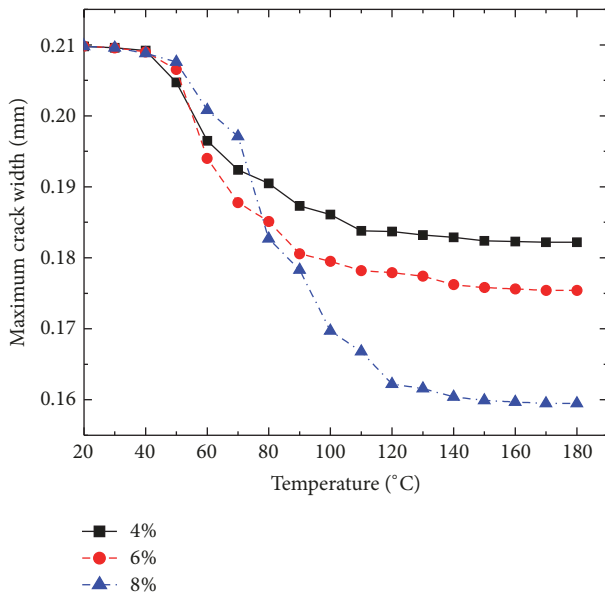


FIGURE 14: The maximum crack widths with different prestrains of SMA wires.

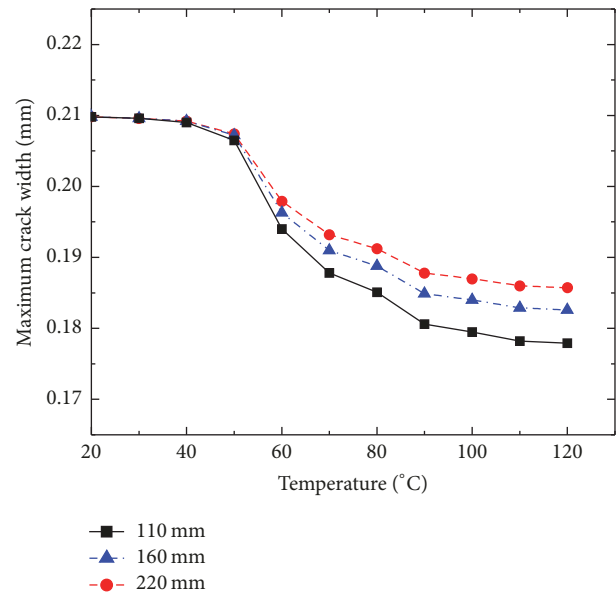


FIGURE 15: The maximum crack widths with different eccentricity of SMA wires.

of the prestrain of SMA wires, the recovery rate of the maximum crack width increases greatly, which explains that the prestrain of SMA wires has a significant influence on the control effect of beam cracks. It is because the larger the prestrain is, the more the austenite transforms during the phase transition and temperature rise, and the greater the recovery stress of SMA wires is, the better the effect of crack control is.

5.2.5. Effect of the Eccentricity of SMA Wires. The eccentricity of SMA wires refers to the distance from SMA wires to the beam neutral axis. The SMA wires with the eccentricity of 110 mm, 160 mm, and 220 mm are used in the models B10, B11, and B2, respectively. The calculation result is shown in Figure 15. In the normal temperature of SMA wires, the maximum crack width of the three beam models is 0.2098 mm. Heating the SMA wires to 120°C, corresponding to the eccentricity from small to large, the maximum crack width of the beam is 0.1857 mm, 0.1826 mm, and 0.1779 mm, and the recovery rate of the maximum crack width is 11.47%,

12.98%, and 15.22%, respectively. Therefore, the maximum crack width recovery rate increases with the increment of the SMA wire eccentricity. The reason is that when the recovery stress is certain, the greater the eccentricity of SMA wires is, the greater the reverse moment is formed, and the more significant the driving effect of SMA wires is, the better the crack control effect of the beam is.

6. Conclusions

Based on the BB-sQRM, a new model is presented in this paper, which is used in the nonlinear analysis for crack control capability of the SMA concrete beam. The discretization of the BB-sQRM is performed with a set of uniformly scattered spline nodes in both two directions of the structure. Then, a transformation relationship is established which is between the node displacement of elements and the spline node displacement of the structure. Through the conversion, the element displacement vector can be expanded to the

vector which has the same dimension as the structural displacement vector. Consequently, it is convenient to generate stiffness matrices and load vectors, and the stiffness equation has a small number of unknowns. Considering the nonlinearity of concrete materials, an explicit form is proposed to express the elastic-plastic constitutive law of concrete, which also simplifies the calculation and programming. Through several numerical examples available in this literature, the convergence and accuracy of the BB-sQRM are proved. The results show that the solutions obtained by the proposed model with relatively few nodes are very close to those given by the space model of ANSYS with a large number of nodes. Therefore, the examples demonstrate the higher efficiency and lower computational cost of the BB-sQRM than those of the FEM simultaneously. Meanwhile, it is shown by the parametric analysis results that the change in thickness of concrete cover and reinforcement ratio makes no difference to the beam crack control capability. And not only the recovery of maximum crack width but also the crack control effect of the SMA concrete beam can be improved usefully by the increase of the depth-span ratio of the beam and prestrain and eccentricity of SMA wires. Thereby, the durability and carrying capacity of the RC structure can be effectively improved.

Conflicts of Interest

The authors declare that there are no conflicts of interest regarding the publication of this article.

Acknowledgments

The work of this paper has been supported by the grants awarded by the National Natural Science Foundation of China (Project no. 11562001), the Guangxi Natural Science Foundation of China (Project no. 2014GXNSFAA118020), and the Systematic Project of Guangxi Key Laboratory of Disaster Prevention and Structural Safety (Project no. 2014ZDX03).

References

- [1] Y. Yao, S. E. Tung, and B. Glisic, "Crack detection and characterization techniques An overview," *Structural Control and Health Monitoring*, vol. 21, no. 9, pp. 1387–1413, 2014.
- [2] C. D. Moen and S. R. Sharp, "Bond properties between concrete and corrosion-resistant reinforcing steels," *ACI Structural Journal*, vol. 113, no. 2, pp. 383–392, 2016.
- [3] A. Michel, B. J. Pease, and A. Peterova, "Penetration of corrosion products and corrosion-induced cracking in reinforced cementitious materials: Experimental investigations and numerical simulations," *Cement Concrete Composites*, vol. 47, no. SI, pp. 75–86, 2014.
- [4] M. A. Adam, M. Said, A. A. Mahmoud, and A. S. Shanour, "Analytical and experimental flexural behavior of concrete beams reinforced with glass fiber reinforced polymers bars," *Construction and Building Materials*, vol. 84, pp. 354–366, 2015.
- [5] B. Han, Y. Wang, S. Dong et al., "Smart concretes and structures: a review," *Journal of Intelligent Material Systems and Structures*, vol. 26, no. 11, pp. 1303–1345, 2015.
- [6] M. M. Sherif, J. Tanks, and O. E. Ozbulut, "Acoustic emission analysis of cyclically loaded superelastic shape memory alloy fiber reinforced mortar beams," *Cement and Concrete Research*, vol. 95, pp. 178–187, 2017.
- [7] B. Silwal, R. J. Michael, and O. E. Ozbulut, "A superelastic viscous damper for enhanced seismic performance of steel moment frames," *Engineering Structures*, vol. 105, pp. 152–164, 2015.
- [8] S. M. R. Khalili, M. Botshekanan Dehkordi, and E. Carrera, "A nonlinear finite element model using a unified formulation for dynamic analysis of multilayer composite plate embedded with SMA wires," *Composite Structures*, vol. 106, pp. 635–645, 2013.
- [9] J. M. Jani, M. Leary, A. Subic, and M. A. Gibson, "A review of shape memory alloy research, applications and opportunities," *Materials and Corrosion*, vol. 56, pp. 1078–1113, 2014.
- [10] E. Patoor, D. C. Lagoudas, P. B. Entchev, L. C. Brinson, and X. Gao, "Shape memory alloys, Part I: General properties and modeling of single crystals," *Mechanics of Materials*, vol. 38, no. 5–6, pp. 391–429, 2006.
- [11] E. Choi, D. J. Kim, J.-H. Hwang, and W. J. Kim, "Prestressing effect of cold-drawn short NiTi SMA fibres in steel reinforced mortar beams," *Smart Materials and Structures*, vol. 25, no. 8, Article ID 085041, 2016.
- [12] H. Li, Z.-Q. Liu, and J.-P. Ou, "Behavior of a simple concrete beam driven by shape memory alloy wires," *Smart Materials and Structures*, vol. 15, no. 4, article no. 017, pp. 1039–1046, 2006.
- [13] Z. Deng, Q. Li, and H. Sun, "Behavior of concrete beam with embedded shape memory alloy wires," *Engineering Structures*, vol. 28, no. 12, pp. 1691–1697, 2006.
- [14] M. K. Kim, D. J. Kim, Y.-S. Chung, and E. Choi, "Direct tensile behavior of shape-memory-alloy fiber-reinforced cement composites," *Construction and Building Materials*, vol. 102, pp. 462–470, 2016.
- [15] L. Sun, D. Liang, Q. Gao, and J. Zhou, "Analysis on factors affecting the self-repair capability of SMA wire concrete beam," *Mathematical Problems in Engineering*, vol. 2013, Article ID 138162, 6 pages, 2013.
- [16] C. Czaderski, M. Shahverdi, R. Brönnimann, C. Leinenbach, and M. Motavalli, "Feasibility of iron-based shape memory alloy strips for prestressed strengthening of concrete structures," *Construction and Building Materials*, vol. 56, pp. 94–105, 2014.
- [17] M. Shin and B. Andrawes, "Emergency repair of severely damaged reinforced concrete columns using active confinement with shape memory alloys," *Smart Materials and Structures*, vol. 20, no. 6, Article ID 065018, 2011.
- [18] A. Abdulridha, D. Palermo, S. Foo, and F. J. Vecchio, "Behavior and modeling of superelastic shape memory alloy reinforced concrete beams," *Engineering Structures*, vol. 49, pp. 893–904, 2013.
- [19] A. R. Khaloo, I. Eshghi, and P. P. Aghl, "Study of behavior of reinforced concrete beams with smart rebars using finite element modeling," *International Journal of Civil Engineering*, vol. 8, no. 3, pp. 221–231, 2010.
- [20] M. S. Alam, M. A. Youssef, and M. Nehdi, "Analytical prediction of the seismic behaviour of superelastic shape memory alloy reinforced concrete elements," *Engineering Structures*, vol. 30, no. 12, pp. 3399–3411, 2008.
- [21] Q. Chen and B. Andrawes, "Finite element analysis of actively confined concrete using shape memory alloys," *Journal of Advanced Concrete Technology*, vol. 12, no. 12, pp. 520–534, 2014.

- [22] P. Lu, F. S. Cui, and M. J. Tan, "A theoretical model for the bending of a laminated beam with SMA fiber embedded layer," *Composite Structures*, vol. 90, no. 4, pp. 458–464, 2009.
- [23] M.-Y. Wang, H.-L. Ji, J.-H. Qiu, and C. Zhang, "Plate stiffness active control with shape memory alloys and layout optimization," *Journal of Vibration and Shock*, vol. 33, no. 23, pp. 30–36, 2014.
- [24] H. Li, Z.-Q. Liu, Z.-W. Li, and J.-P. Ou, "Study on damage emergency repair performance of a simple beam embedded with shape memory alloys," *Advances in Structural Engineering*, vol. 7, no. 6, pp. 495–501, 2004.
- [25] S.-B. Li, C.-M. Mo, and Q.-G. Liang, "Recovery performance of shape memory alloy and its application in repairing cracks of concrete beams," *Concrete*, vol. no. 4, pp. 68–73, 2015.
- [26] S. B. Li, Q. G. Liang, and J. P. Li, "Finite Element Analysis for the Crack Self-Repairing Behavior of the Concrete Beam Embedded Shape Memory Alloy," *Applied Mechanics and Materials*, vol. 507, pp. 455–459, 2014.
- [27] V. P. Nguyen, T. Rabczuk, S. Bordas, and M. Duflot, "Meshless methods: a review and computer implementation aspects," *Mathematics and Computers in Simulation*, vol. 79, no. 3, pp. 763–813, 2008.
- [28] L. X. Peng, Y.-P. Tao, H.-Q. Li, and G.-K. Mo, "Geometric non-linear meshless analysis of ribbed rectangular plates based on the FSDT and the moving least-squares approximation," *Mathematical Problems in Engineering*, vol. 2014, Article ID 548708, 13 pages, 2014.
- [29] L. X. Peng, "Free Vibration Analysis of Symmetrically Laminated Folded Plate Structures Using an Element-Free Galerkin Method," *Mathematical Problems in Engineering*, vol. 2015, Article ID 124296, 13 pages, 2015.
- [30] S.-B. Li, H. Wu, and C.-M. Mo, "Dynamic analysis of thick/thin piezoelectric FGM plates with spline meshless method," *Journal of Vibration and Shock*, vol. 36, no. 7, pp. 116–122, 2017.
- [31] P. Liu, K. Lin, H. Liu, and R. Qin, "Free Transverse Vibration Analysis of Axially Functionally Graded Tapered Euler-Bernoulli Beams through Spline Finite Point Method," *Shock and Vibration*, vol. 2016, Article ID 5891030, 23 pages, 2016.
- [32] S.-B. Li, L.-X. Huang, L.-J. Jiang, and R. Qin, "A bidirectional B-spline finite point method for the analysis of piezoelectric laminated composite plates and its application in material parameter identification," *Composite Structures*, vol. 107, no. 1, pp. 346–362, 2014.
- [33] R. Qin, *Computational Structure Mechanics*, Guangxi Normal University Press, Guilin, China, 1997.
- [34] A. C. T. Chen and W. F. Chen, "Constitutive relations for concrete," *Journal of Engineering Mechanics*, vol. 101, no. EM4, pp. 465–481, 1975.
- [35] R. Q. *Nonlinearity Analysis of Engineering Structures*, Science Press, Beijing, China, 2006.
- [36] J.-Q. Jiang and X.-Z. Lu, *Finite Element Analysis of Concrete Structures*, Tsinghua University Press, Beijing, China, 2013.
- [37] GB, 50010-2010, Code for Design of Concrete Structures, General Administration of Quality Supervision, Inspection and Quarantine of the People's Republic of China (AQSIQ), 2010.

